clearly unrealistic procedure here.

[31] N. V. Smith and R. Y. Koyama (unpublished).

[32] E. T. Goodwin, Proc. Cambridge Phil. Soc. 35, 205 (1939). We modify his model [following A. Many *et al.*, *Semiconductor Surfaces* (North-Holland, Amsterdam, 1965), p. 174, whose notation we adopt] to refer to a semi-infinite crystal rather than one of N layers.

[33] D. Beaglehole and E. Erlbach, Solid State Commun. 8, 255 (1970).

[34] N. V. Smith, in Ref. 6.

[35] W. F. Krowlikowski and W. E. Spicer, Phys. Rev. 185, 882 (1969).

[36] The strong growth in width on the high-energy side of the bulk-state yield is another misleading aspect of the model.

[37] F. Forstmann and V. Heine, Phys. Rev. Letters 24, 1419 (1970).

[38] F. Forstmann and J. B. Pendry, Z. Physik 235, 75 (1970).

[39] The data for $b=\frac{3}{4}a$ were essentially identical (somewhat below) those for $b=\frac{1}{2}a$..

[40] The reason for the difference between this curve and the one of Fig. 6 is that we have imposed the condition of *escape after excitation.*

[41] E. O. Kane, Phys. Rev. 175, 1039 (1968).

[42] A. Messiah, Ref. 16, p. 106.

[43] C. Herring and M. H. Nichols, Rev. Mod. Phys. 21, 185 (1949).

[44] L. A. MacColl, Phys. Rev. 56, 699 (1939).

[45] L. A. MacColl, Bell System Tech. J. 30, 888 (1951).

[46] N. F. Mott and H. Jones, *Properties of Metals and Alloys* (Dover, New York, 1958), p. 68.

[47] M. Skibowski *et al.*, Z. Physik 211, 343 (1968); S. V. Pepper, J. Opt. Soc. Am. 60, 805 (1970).

[48] Some progress is possible in perturbation theory; see Ref. 10.

PHYSICAL REVIEW B VOLUME 3, NUMBER 8 15 APRIL 1971

Doppler-Shifted Acoustic Cyclotron-Resonance Studies in Magnesium†

R. W. Stark
The James Franck Institute and the Department of Physics,
The University of Chicago, Chicago, Illinois 60637
The University of Arizona, Department of Physics, Tucson, Arizona 85721

and

J. Trivisonno and R. E. Schwarz
The Department of Physics, John Carroll University, Cleveland, Ohio 44118

(Received 12 October 1970)

A study of Doppler-shifted acoustic cyclotron resonance in magnesium is reported. The results are compared with the quantitative predictions of band-structure calculations based on the nonlocal orthogonalized-plane-wave pseudopotential model Hamiltonian for magnesium reported by Kimball, Stark, and Mueller. The dominant family of resonances yield an experimental value for the rate of change of the cross-sectional area of the Fermi surface with the component of the electron wave vector along the magnetic field of 0.80 ± 0.02 a.u. compared with a theoretical prediction of 0.793 a.u. The experimental cyclotron mass of 0.78 ± 0.05 free-electron masses compares with a prediction of 0.78 ± 0.02 free-electron masses. The expectation value of the electron drift velocity along the magnetic field determined from experiment is 3.65×10^7 cm/sec, while theory predicts 3.73×10^7 cm/sec. The relative amplitudes of the successive resonances in the attenuation are in the ratio 1:0.64:0.41 compared with a predicted ratio of 1:0.645:0.344. At 4.2 °K the electron mean free path for small-angle scatter determined from the resonance line shape was 1.4 mm compared with a sample thickness of 1.9 mm. At the lowest temperatures used with the experiment, the mean free path becomes equivalent to the sample thickness.

I. INTRODUCTION

The attenuation of a sound wave in a pure metal at low temperatures is dominated by the interaction of the wave with the conduction electrons. The first conclusive experimental evidence for the importance of the role played by the conduction electrons was the observation of a sharp reduction in the attenuation upon crossing the transition from the normal state into the superconducting state.[1,2] Shortly after the initial observations it was found that the attenuation could be effected in a nonmonotonic way by the application of a magnetic field of varying strength and orientation.[3]

Various aspects of the physical manifestations of the interaction of sound waves with electrons orbiting in the presence of an applied magnetic field $\vec{H}$ have been discussed in some detail by several authors.[4-7] The phenomenon of "geometric resonance" has been extensively utilized to determine dimensions of Fermi surfaces.[8] In that experiment, $\vec{H}$ is applied perpendicular to the sound wave vector $\vec{q}$ and the resonances are spatial rather than temporal. Although geometric-resonance studies have played an important historical role in increasing our understanding of electrons in metals, they have recently been cast in a somewhat secondary position by the over-all power of the de Haas–van Alphen technique.[9]

Another resonance, Doppler-shifted acoustic cyclotron resonance, occurs when $\vec{H}$ is more nearly parallel to $\vec{q}$.[5,10–12] These resonances are temporal resonances between the electron cyclotron motion and the periodic sound wave fronts as seen from a reference frame moving along the magnetic field lines with the electron. In contrast with geometric resonances, Doppler-shifted acoustic cyclotron resonances have, to date, yielded only token amounts of pertinent information. The essential reason for this relates to the fact that the former experiment yields data which can be interpreted in terms of extremal dimensions of the Fermi surface whereas the data from the latter require interpretation in terms of extremal derivatives of the Fermi surface.

Until very recently our knowledge of Fermi-surface geometry has been sufficiently inaccurate to preclude much more than a qualitative interpretation of Doppler-shifted acoustic cyclotron-resonance data. A major aspect of this problem is the existence of symmetry-related selection rules[13] which prevent a straightforward interpretation of the data. This will be discussed in more detail in Sec. II.

One of the metals for which the Fermi surface and energy-band structure is well known is magnesium. Reference 14 describes the details of the orthogonalized-plane-wave (OPW) model Hamiltonian used to represent the electron-ion interaction as well as the comparison of the resulting Fermi-surface model with experimental data. It was shown that in every instance the agreement was within the experimental error. Since then the OPW model has been used to generate a dense array of electron wave vectors $\vec{k}$ for the magnesium Fermi surface.[15] These points satisfy the energy relation $\vec{k}(E)=\vec{k}(E_F)$, where E_F is the Fermi energy; tabulated also are the local Fermi velocities $\vec{V}_{\vec{k}}(E_F)$. The density is such that each point of the array represents less than 10^{-5} of the surface area of the single OPW spherical Fermi surface.

This array has been used to calculate the dynamic response of the conduction electrons to applied electric and magnetic fields. In every case treated thus far it has yielded agreement with experiment. We thus expect that with this model the results of an investigation of the Doppler-shifted acoustic cyclotron resonance in magnesium should be amenable to quantitative interpretation.

Since single crystals of high-purity magnesium having relatively long electron mean free paths at helium temperatures were available, we undertook an investigation of the Doppler-shifted acoustic cyclotron resonance in order to test the quantitative accuracy of the existing theoretical understanding of this phenomenon.

II. THEORY

A theoretical treatment of the general interaction of conduction electrons and acoustic waves in the presence of a magnetic field is complicated by several factors.[16] In general the polarization $\hat{\epsilon}$ of the acoustic vibration in the crystal will not normally be either parallel to $\vec{q}$ (longitudinal wave) or perpendicular to $\vec{q}$ (transverse wave) but will instead be some linear combination of these; when $\vec{q}$ is placed parallel to a crystal axis of twofold or higher symmetry or placed in a symmetry plane a pure vibrational mode can be generated.

In addition it is only for the case of a pure longitudinal mode that one can describe the interaction of an electron with a sound wave in terms of a conservative field of force. For clarity our discussion will be restricted to the particular case of a longitudinal sound wave propagated parallel to a crystal axis of s-fold symmetry, where $s \geq 2$.

The motion of an electron in an applied magnetic field is a periodic function of time. The fundamental time unit of its motion is the cyclotron frequency ω_c. Thus, at a time t, the electron's velocity $\vec{V}(t)$ can be expressed as a complex Fourier series

$$\vec{V}(t)=\sum_{n=-\infty}^{+\infty}\vec{V}_n e^{in\omega_c t}\ . \tag{1}$$

In (1) the fact that the velocity $\vec{V}(t)$ is real imposes the condition that $\vec{V}_{-n}=\vec{V}_n^{\,*}$. The position of the electron in real space $\vec{r}(t)$ is given by

$$\vec{r}(t)=\int \vec{V}(t)\,dt\ . \tag{2}$$

If $\vec{r}(0)=0$ and $\omega_c t \gg 2\pi$, Eq. (2) can be approximated quite accurately by $\vec{r}(t)=\vec{V}_0 t$, where $\vec{V}_0$, the $n=0$ term in Eq. (1), is the expectation value of the electron's drift velocity in $\vec{H}$.

The interaction of the electron with a longitudinal sound wave of frequency ω propagated along a crystal symmetry axis can be represented by a periodic position-dependent conservative force on the electron

$$\vec{F}=F_0\hat{q}\,e^{i[\omega t-\vec{q}\cdot\vec{r}(t)]}\ , \tag{3}$$

where ω is the sound wave frequency. Equation (3) assumes that F_0 is independent of the position of the electron on its orbit in $\vec{k}$ space. In principle $F_0=F_0(\vec{k})$ or, in our representation, $F_0=F_0(t)$ since $\vec{k}=\vec{k}(t)$. However, for a metal whose band structure and Fermi surface are as free-electron-like as are magnesium's, we anticipate only small variations in F_0 around the orbit. In any case variations in F_0 will not affect any of the following discussion with the possible exception of the relative amplitude of the successive resonances in a family of Doppler-shifted acoustic cyclotron resonances. We will return to this point later. Assuming that F_0 is constant, the rate at which energy is transferred from the wave to the electron is

$$\frac{dE}{dt} = \vec{F}\cdot\vec{V}(t) = \sum_{n=-\infty}^{\infty} F_0\vec{V}_n\cdot\hat{q}e^{i(\omega+n\omega_c-\vec{q}\cdot\vec{V}_0)t} . \tag{4}$$

If the average electron relaxation time τ is isotropic around the electron's orbit, the total average energy transferred to the electron from the sound wave is obtained by integrating the probability weighted power along the past trajectory, i.e.,

$$\Delta E = \int_{-\infty}^{0} \frac{dE}{dt} e^{t/\tau} dt . \tag{5}$$

Thus if one substitutes Eq. (4) into Eq. (5) and integrates, one obtains

$$\Delta E = \sum_{n=-\infty}^{+\infty} \frac{F_0\vec{V}_n\cdot\hat{q}}{1/\tau + i(\omega + n\omega_c - \vec{q}\cdot\vec{V}_0)} . \tag{6}$$

The absorption of energy is resonant whenever $n\omega_c = \vec{q}\cdot\vec{V}_0 - \omega$, that is, whenever some harmonic of the cyclotron frequency ω_c is equal to the Doppler-shifted sound wave frequency $\vec{q}\cdot\vec{V}_0 - \omega$. In addition, the amount of energy absorbed at resonance is proportional to $\vec{V}_n\cdot\hat{q}$.

Equation (6) gives the energy exchanged as a function of $\vec{H}$ for a single orbit; in practice, one must multiply (6) by an appropriate density-of-states factor and integrate over all orbits to get the total energy exchange. The only resonances which will survive this integration to ultimately appear in experimental data are those which are associated with singularities in this density of states. These singularities are readily related to Fermi-surface geometry.

Figure 1 shows the projection of a typical electron's orbital path onto the plane containing $\vec{q}$ and $\vec{H}$. Shown also are a sequence of sound wave fronts having an effective wavelength λ_{eff}. As seen in this projection the electron performs a complicated harmonic motion about the magnetic field line; this motion is repeated in time with period $2\pi/\omega_c$. It propagates a distance

$$L = (2\pi/\omega_c)\vec{V}_0\cdot\hat{q} \tag{7}$$

in the direction of $\vec{q}$ during each cycle of its motion. A resonance occurs whenever L is equal to some integer multiple of λ_{eff}, i.e., $L = n\lambda_{\text{eff}}$. The significance of the effective wavelengths results from the fact that in the time $2\pi/\omega_c$ that it takes for the electron to travel the distance L, the sound wave fronts have propagated a distance $\lambda(\omega/\omega_c)$. Thus

$$n\lambda_{\text{eff}} = (n - \omega/\omega_c)\lambda = (2\pi/\omega_c)\vec{V}_0\cdot\hat{q} , \tag{8}$$

where λ is the actual sound wavelength.

For every electron which moves on an orbit against the sound waves as described above, there is another electron on an identical type orbit but inverted through the origin of $\vec{k}$ space which moves with the sound wave fronts. For this electron the effective wavelength is increased by the term involving ω/ω_c. Combining these symmetrical orbits and multiplying by ω_c/λ we have

$$\vec{V}_0\cdot\vec{q} \pm \omega = n\omega_c . \tag{9}$$

Equation (9) is identical to the resonance condition specified by Eq. (6).

Nowhere has the above discussion required the imposition of any restrictions related to orbit geometry, that is, to whether the electron orbit in $\vec{k}$ space is closed or open. In addition, no restriction has been made dealing with the symmetry of the orbit about the magnetic field direction. The distinctions which classify these different types of orbits are distinctions that state which of the Fourier coefficients $\vec{V}_n$ of Eq. (1) must be zero. In order to consider these distinctions it is convenient to establish the following Cartesian coordinate system: Let $\hat{1}$ be specified by the direction of $\vec{H}$, with $\hat{2}$ and $\hat{3}$ in the plane perpendicular to $\vec{H}$. Thus a typical Fourier coefficient can be represented by its components along these unit vectors, i.e., $\vec{V}_n = V_1^n\,\hat{1} + V_2^n\,\hat{2} + V_3^n\,\hat{3}$. The distinction between open and closed orbits results in a restriction on the $n = 0$ coefficients, since the drift velocity ($n = 0$ coefficients) of the electron in the 2-3 plane must be zero by definition for closed orbits while it is unrestricted for open orbits. In fact, for an open orbit directed

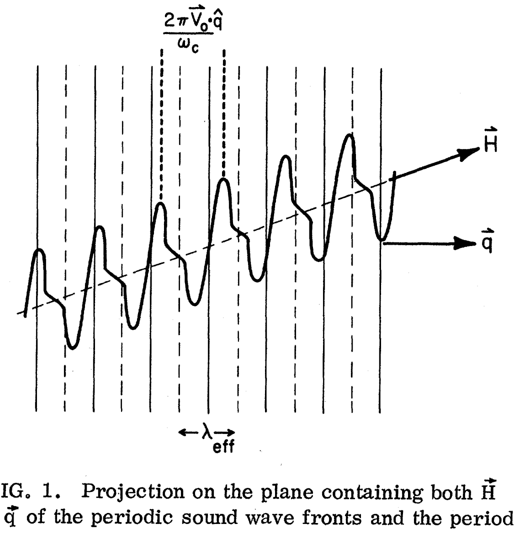

FIG. 1. Projection on the plane containing both $\vec{H}$ and $\vec{q}$ of the periodic sound wave fronts and the periodic orbit path of a typical electron on its trajectory.

TABLE I. Restrictions on the values of the complex Fourier coefficients of $\vec{V}(t)$ due to orbit geometry.

Type of orbit Open	Closed Onefold	Twofold	Threefold
(V_1^0, V_2^0, V_3^0)		$(V_1^0, 0, 0)$	
(V_1^1, V_2^1, V_3^1)	(V_1^1, V_2^1, V_3^1)	$(0, V_2^1, V_3^1)$	$(0, V_2^1, V_3^1)$
(V_1^2, V_2^2, V_3^2)	(V_1^2, V_2^2, V_3^2)	$(V_1^2, 0, 0)$	$(0, V_2^2, V_3^2)$
(V_1^3, V_2^3, V_3^3)	(V_1^3, V_2^3, V_3^3)	$(0, V_2^3, V_3^3)$	$(V_1^3, 0, 0)$
(V_1^4, V_2^4, V_3^4)	(V_1^4, V_2^4, V_3^4)	$(V_1^4, 0, 0)$	$(0, V_2^4, V_3^4)$
(V_1^5, V_2^5, V_3^5)	(V_1^5, V_2^5, V_3^5)	$(0, V_2^5, V_3^5)$	$(0, V_2^5, V_3^5)$
(V_1^6, V_2^6, V_3^6)	(V_1^6, V_2^6, V_3^6)	$(V_1^6, 0, 0)$	$(V_1^6, 0, 0)$
(V_1^7, V_2^7, V_3^7)	(V_1^7, V_2^7, V_3^7)	$(0, V_2^7, V_3^7)$	$(0, V_2^7, V_3^7)$
(V_1^8, V_2^8, V_3^8)	(V_1^8, V_2^8, V_3^8)	$(V_1^8, 0, 0)$	$(0, V_2^8, V_3^8)$

at an arbitrary angle in the 2-3 plane, there are no restrictions placed on V_1^n, V_2^n, or V_3^n for any value of n. However, for closed orbits the V^n are restricted by the symmetry of the orbit about $\vec{\mathrm{H}}$. For example, $V_1(t)$ has the same symmetry as the orbit. If the orbit has s-fold symmetry, the fundamental time unit describing the repetition frequency of $V_1(t)$ is not ω_c but is instead given by $s\omega_c$. Thus the Fourier expansion of $V_1(t)$ that is given in Eq. (1) will yield nonzero coefficients V_1^n only for $n = ms$, $m = 0, 1, 2, \ldots$. The restrictions placed on V_2^n and V_3^n in this case are different, since it is the magnitude of the velocity in the 2-3 plane, $V_{23}(t) = [V_2(t)^2 + V_3(t)^2]^{1/2}$, that has the symmetry of the orbit. This is satisfied if V_2^n and V_3^n are nonzero only when $n = ms \pm 1$, $m = 0, 1, 2, \ldots$. A summary of the restrictions imposed on the V_i^n for closed orbits with up to threefold symmetry is given in Table I. It is important to note that these restrictions result only from geometrical considerations; they are not related to quantum mechanics or energy and momentum conservation rules.

Since in all cases for closed orbits $\vec{\mathrm{V}}_0 = V_1^0 \hat{1}$, we can use a simple geometrical relation due to Harrison[17] and rewrite Eq. (9) as

$$L = \frac{\hbar c}{eH}\left(\frac{\partial A}{\partial k_H}\right)\hat{\mathrm{H}}\cdot\hat{q} = \left(n \pm \frac{\omega}{\omega_c}\right)\lambda\,, \tag{10}$$

where A is the cross-sectional area of the electron orbit in $\vec{\mathrm{k}}$ space and for clarity we have replaced $\hat{1}$ by $\hat{H}$.

For a typical metal $\omega/\omega_c \approx 10^{-2}$, so that Eq. (10) describes a resonance in H with two peaks split by about 1% of the central-field value. Families of resonances in the experimental data will occur when $L = L(k_1)$ is extremal in k_1, i.e., when $\partial A/\partial k_1$ is extremal; this quantity can then be determined from the location of the resonance. The value of the splitting of the two peaks gives a value for m^* which together with the value of $\partial A/\partial k_1$ determines V_1^0.

For convenience we will anticipate the results of our study of Doppler-shifted acoustic cyclotron resonance in magnesium and discuss in this section the origin and geometry of the orbits which contribute the largest family of resonances to the experimental data. The reader is referred to Ref. 8 for a complete description of the single-OPW Fermi-surface model for magnesium and to Ref. 14 for a description of the OPW model Hamiltonian that was used to perturb the single OPW Fermi surface into complete agreement with experimental data. Reference 15 describes the numerical techniques that were developed to generate and use an array of $\vec{\mathrm{k}}$ vectors and velocities $\vec{\mathrm{V}}_{\vec{\mathrm{k}}}$ to allow accurate representation of the OPW model Hamiltonian.

Figure 2 shows most of the second-band hole surface (the monster) together with the first Brillouin zone and some of its symmetry points. The cross-sectional area of a segment of the monster enclosed by a dog-bone-shaped orbit is shown; the $\hat{1}$, $\hat{2}$, $\hat{3}$ coordinate system follows the specifications given above. In this particular case, $\hat{1}$ is parallel to ΓM, i.e., $\vec{\mathrm{H}}$ is parallel to a $\langle 10\bar{1}0\rangle$ crystallographic direction, $\hat{2}$ is parallel to Γk, and $\hat{3}$ is parallel to ΓA. This type of orbit is representative of those responsible for the dominant family of resonances in the experimental data.

Figure 3 shows, as a function of k_1, the theoretical values of the cross-sectional area in the 2-3 plane, $A(k_1)$, of the second-band hole surface shown in Fig. 2. The plane $k_1 = 0$ is chosen to include Γ, the center of the Brillouin zone. For this orientation of $\vec{\mathrm{H}}$, the orbits on the Fermi surface for $0.0 \le k_1 \le 0.024$ a.u. are not closed but are open and hence have no definable cross-sectional area. Saddle points relative to the 2-3 plane exist on the Fermi surface at $k_1 = 0.024$, 0.37, 0.47, 0.545, and 0.576 a.u. At

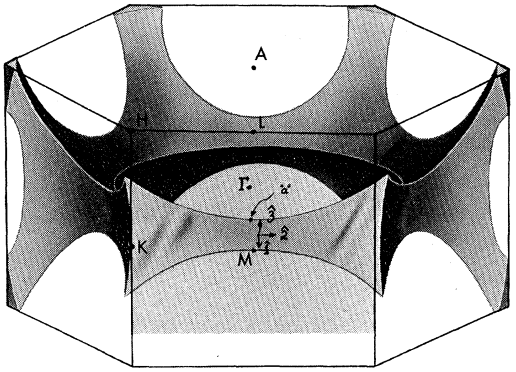

FIG. 2. Portion of the second-band hole surface, the monster, showing the location of a typical dog-bone-type orbit. The $\hat{1}$, $\hat{2}$, $\hat{3}$ coordinate system is defined in the text.

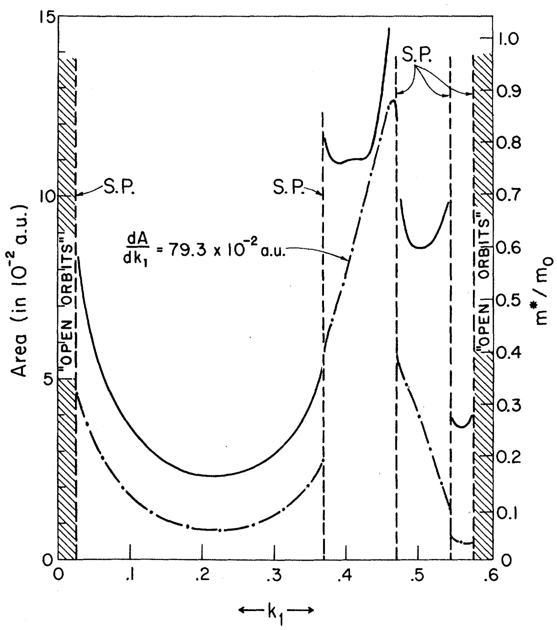

FIG. 3. Theoretical cross-sectional area and effective cyclotron mass of the second-band hole surface as a function of k_1, where k_1 is the component of the electron wave vector along the 1 axis shown in Fig. 2 and is measured in a.u. S. P. indicates saddle-point locations. The solid curve refers to the effective cyclotron mass; the broken curve refers to the cross-sectional area.

these points the orbit shape changes, the cyclotron mass $m^*(k_1)$ becomes infinite, $dA(k_1)/dk_1$ becomes infinite, and $A(k_1)$ changes by exactly a factor of 2. The dog-bone-shaped orbit shown in Fig. 2 is the typical orbit for $0.37 \leq k_1 \leq 0.47$ a.u. Notice in Fig. 3 that for k_1 in this range, $A(k_1)$ is an almost exactly linear function of k_1. In fact, for $0.38 \leq k_1 \leq 0.44$ a.u., $\partial A(k_1)/\partial k_1$ is constant and has the value 79.3×10^{-2} a.u. Rather more than 10% of all the states on the Fermi surface lie in this band of constant $\partial A(k_1)/\partial k_1$ and its symmetrically equivalent band at $-0.38 \geq k_1 \geq -0.44$ a.u. With so many states participating in forming the resonance it is not surprising that these orbits dominate the experimental data for Doppler-shifted acoustic cyclotron resonance in magnesium.

Also shown in Fig. 3 is $A(k_1)$ for $0.024 \leq k_1 \leq 0.37$ a.u. $A(k_1)$ shows an absolute minimum at $k_1 = 0.215$ a.u., but nowhere in this region is $\partial A(k_1)/\partial k_1$ constant. Hence this region will not contribute any resonances.

For $0.47 \leq k_1 \leq 0.545$ a.u., $A(k_1)$ varies nearly linearly with k_1 but does not have an inflection point. $dA(k_1)/dk_1$ increases uniformly from a value of 0.52 a.u. at $k_1 = 0.47$ a.u. to a value of 0.66 a.u. at $k_1 = 0.545$ a.u.

For $0.545 \leq k_1 \leq 0.576$ a.u., $A(k_1)$ does not have a constant rate of change with k_1; for $0.576 \leq k_1 \leq 0.604$ a.u., the orbits on the Fermi surface are open and have no definable cross-sectional area.

The theoretical value[14] of $m^*(k_1)$ including a net enhancement factor of 1.26 is shown in Fig. 3. Note that although $m^*(k_1)$ follows the general variation of $A(k_1)$ for most values of k_1, it is essentially constant over just that region which is expected to contribute the large resonance. The value in the resonance region is $m^*(k_1) = (0.78 \pm 0.02) m_0$, where m_0 is the free-electron rest mass.

We can insert the theoretical value of $\partial A(k_1)/\partial k_1$ and $m^*(k_1)$ into Eq. (10) together with the appropriate value of λ to predict the values of H for the experimental resonances. In addition, knowing the location in k_1 of the resonance region we can calculate $\vec{V}(t)$ for a typical orbit and Fourier analyze it in accord with Eq. (1). Figure 4 shows for $k_1 = 0.40$ a.u., $V_1(t)$, $V_2(t)$, and $V_3(t)$ for the dog-bone-shaped orbit shown in Fig. 2. The time scale is $\omega_c t$ so that Fig. 4 shows the evolution of the $V_i(t)$ for one cyclotron period. The starting point at $t = 0$ coincides with point a on the orbit in Fig. 2. Notice in Fig. 2 that the $\hat{1}$ axis is an axis of twofold symmetry; this information also appears in Fig. 4 in that $V_1(t)$ is doubly periodic in the cyclotron period. The restrictions on the Fourier coefficients of $\vec{V}(t)$ for this case are given in Table

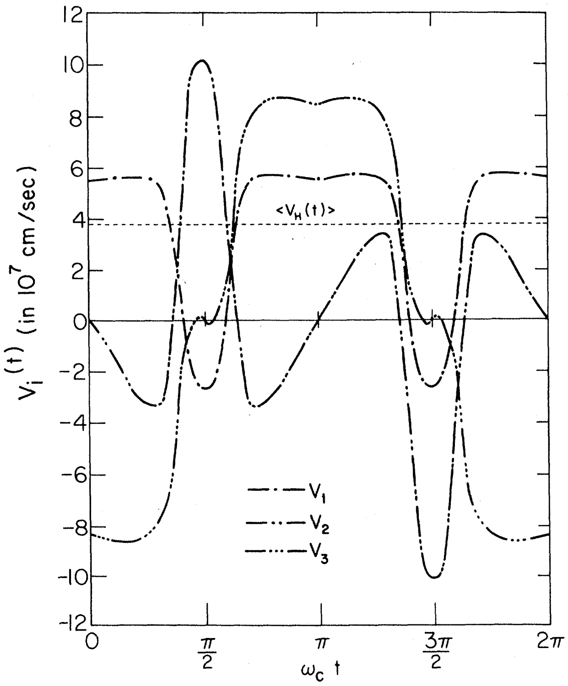

FIG. 4. $V_1(t)$, $V_2(t)$, and $V_3(t)$ velocity components for one cycle of the periodic cyclotron motion for the dog-bone orbit shown in Fig. 2. The expectation value $\langle V_H(t) \rangle$ of the drift velocity along $\vec{H}$ is also shown.

TABLE II. Complex Fourier coefficients of $V_1(t)$, $V_2(t)$, and $V_3(t)$ for the dog-bone-shaped orbit (in 10^7 cm/sec).

n	V_1^n	V_2^n	V_3^n
0	3.73	0	0
1	0	$-0.50e^{i\pi/2}$	-2.46
2	0.82	0	0
3	0	$1.26e^{i\pi/2}$	0.26
4	-0.52	0	0
5	0	$0.79e^{i\pi/2}$	0.14
6	0.28	0	0
7	0	$-0.32e^{i\pi/2}$	-0.28
8	-0.10	0	0

I. The actual value of the first several Fourier coefficients of the $V_i(t)$ shown in Fig. 4 are listed in Table II. These velocities are the band-structure velocities divided by the enhancement factor of 1.26.

It is apparent from Eq. (6) that to a good approximation the relative amplitudes of successive resonances in a family of resonances depends only on $\vec{V}_n\cdot\hat{q}$. If we describe $\hat{q}$ in terms of its direction cosines $(\gamma_1, \gamma_2, \gamma_3)$ relative to the $\hat{1}, \hat{2}, \hat{3}$ axis system, then in general,

$$\vec{V}_n\cdot\hat{q}=\gamma_1 V_1^n+\gamma_2 V_2^n+\gamma_3 V_3^n .$$

For the case of $\vec{H}\parallel\hat{q}$, one has $\gamma_1=1$, $\gamma_2=\gamma_3=0$, and $\vec{V}_n\cdot\hat{q}=V_1^n$. The resonances for $n=1, 3, 5, 7\ldots$ are missing for the dog-bone-shaped orbit when $\vec{H}\parallel\hat{q}$, while for $n=2, 4, 6, 8, \ldots$ the relative amplitude of the energy attenuation at each resonance should be proportional to V_1^n. In contrast, suppose that $\hat{q}$ is placed along a $[10\bar{1}0]$-type axis different from that along which $\vec{H}$ is placed. That is, $\hat{q}$ is 60° from $\vec{H}$ in the basal plane; for this case, $\gamma_1=\frac{1}{2}$, $\gamma_2=\frac{1}{2}\sqrt{3}$, and $\gamma_3=0$. The resonances for $n=1, 3, 5, 7, \ldots$ are no longer missing – their amplitude is proportional to $\frac{1}{2}\sqrt{3}\ V_2^n$. The resonances for $n=2, 4, 6, 8, \ldots$ are now proportional to $\frac{1}{2}V_1^n$. We will comment on the extent of the agreement between experimental data and these predictions in Sec. IV.

III. EXPERIMENTAL PROCEDURE

The conventional pulse-echo technique was used to study Doppler-shifted acoustic cyclotron resonances in the frequency range 30–470 MHz.[18] Longitudinal sound waves were propagated along a $[10\bar{1}0]$ crystallographic axis of magnesium specimens approximately 2 mm in length. Two different crystals were used in this experiment; one of these was strained sufficiently to be observed with x-ray-diffraction measurements. These crystals were spark planed to within 0.5° of a $(10\bar{1}0)$ plane.

X-cut coaxially plated 10-MHz quartz transducers were used to transmit and receive the signals. The transmitting transducer was bonded to a Z-cut quartz delay rod using 6×10^4 cstoke (1 stoke = 1 cm^2/sec) Dow-Corning fluid. This was also found satisfactory to bond the magnesium to the delay rod. The second transducer was then applied to the magnesium specimen; since magnesium oxidizes in air it was found necessary before applying the transducer to first lightly lap the crystals with jeweler's rouge in mineral oil on a flat glass plate in order to obtain a good acoustic bond.

The acoustic probe in which the samples were mounted was designed to allow the propagation direction of sound waves to be brought parallel to the magnetic field direction. An optical lever system was used to align the vertical axis of the acoustic probe to within 0.5° of the Dewar axis to ensure that $\vec{q}$ be parallel to $\vec{H}$ to better than 0.5°. Alignment of the other crystallographic axes was accomplished using a flat on the specimen as a reference. The final alignment was obtained by studying the anisotropy in the high-field attenuation. The symmetry observed in these plots was used to adjust the final orientation of $\vec{q}$ relative to $\vec{H}$. Typical plots of the anisotropy of the high-field attenuation are shown in Fig. 5.

An autocorrelation system employing a phase-sensitive detection scheme[19] was used to record the variation in signal height as a function of magnetic field strength. A dc output voltage was available at the phase-sensitive detector proportional to the amplitude of the received acoustic signal. This voltage was applied to the y axis of the chart recorder. A magnet sweep generator was used to drive a Harvey Wells magnet linearly with time and also to supply an output voltage proportional to the field for the recorder. Hence a plot of relative amplitude attenuation vs magnetic field strength could be made automatically.

The phase-sensitive detector was equipped with several integrating time constants which allowed noise to be averaged out of the received signal. However, the position and amplitude of the resonances were found to be influenced both by integration time and sweep rate. A 1-kG/min sweep rate and a 30-msec integration time were found satisfactory and produced no measurable difference in either the shape or position of the resonance peaks in the attenuation when the field was swept in an increasing or decreasing mode.

The magnetic fields at which the resonances occurred were measured with a 0.1% Rawson rotating gaussmeter. Since the splitting in the resonances is related to m^*, it was necessary to measure the positions of the resonant peaks very accurately. The calibrations were made by offsetting the x axis of the chart recorder in order to obtain maximum sensitivity in the field range of interest.

Relative attenuation calibrations were made using

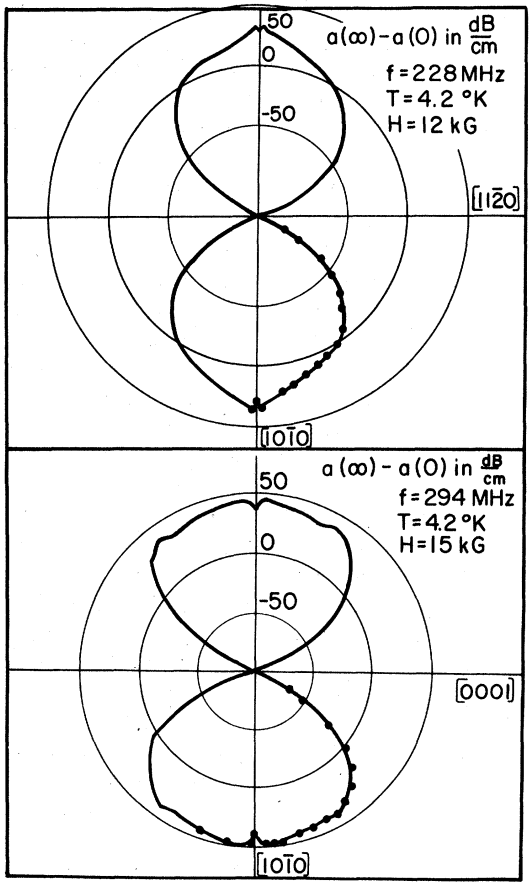

FIG. 5. Field-rotation diagrams showing the anisotropic dependence of the acoustic attenuation on the orientation of the magnetic field relative to the crystallographic axes. $\vec{q}$ is parallel to ⟨10$\bar{1}$0⟩.

an externally pulsed Hewlett Packard 608 D VHF signal generator to obtain a comparator pulse set to the same frequency as the acoustic signal. The comparator was then fed into the receiver and its amplitude varied using the calibrated piston attenuator. The piston attenuator could then be used to calibrate the y axis of the chart recorder to ± 0.2 dB.

The 608 D VHF oscillator was also used to determine the frequency to about 0.3%.

IV. EXPERIMENTAL RESULTS

The characteristic sharp resonant peaks in the ultrasonic attenuation due to Doppler-shifted acoustic cyclotron resonances were observed in both magnesium crystals with $\vec{q}$ parallel to [10$\bar{1}$0]. Typical data taken at 4.2 °K for the case in which $\vec{H}$ is essentially parallel to $\vec{q}$ is shown in Fig. 6 where the relative amplitude attenuation is plotted as a function of magnetic field strength. The essential differences between the two curves shown in Fig. 6 results from the fact that the acoustic frequency was 410 MHz for the upper curve but only 290 MHz for the lower curve. Equation (10) shows that the magnetic field strength at which a resonance occurs is directly proportional to the sound wave frequency; thus a proportionate change was made in the horizontal gain of the x-y recorder to compensate for the sound frequency change in order to make the two data traces more directly comparable. The abscissa and ordinate of the upper curve are the upper and right scales, respectively; the abscissa and ordinate of the lower curve are the lower and left scales, respectively. Sharp resonances in the attenuation are visible in both curves including at least four harmonics of the strong resonance at 3.4 kG on the upper curve. These resonances are periodic in H^{-1} and it is this particular family of resonances which we associate with the dog-bone-shaped orbit shown in Fig. 2. The even-number indexing of the resonances that is indicated in the figure results from the twofold symmetry of that orbit.

The Doppler splitting in Eq. (10) is apparent in the data. The data for the two frequencies are remarkably similar; about the only difference in the two curves is the sharper more pronounced character of the resonances at higher frequencies. This results solely from the effects of the electron mean free path l compared with the sound wavelength λ. The fractional fullwidth at half-maximum of a reso-

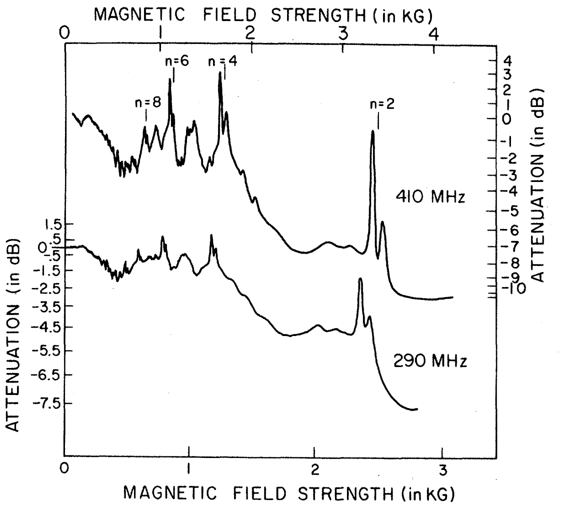

FIG. 6. Acoustic attenuation for longitudinal waves propagated along ⟨10$\bar{1}$0⟩ as a function of magnetic field strength for $\vec{H}$ along ⟨10$\bar{1}$0⟩. The upper curve was taken at 410 MHz; the lower curve was taken at 290 MHz; both curves were taken at 4.2 °K. The upper and right scales refer to the 410-MHz data; the lower and left scales refer to the 290-MHz data. Note that the curves shown above are a draftsman's retracing of the original data. The numbers quoted in the text were measured from the original data.

nance line is $\Delta H/H = \lambda/l$. For the $n=2$ line the fractional full width is 10.4×10^{-3} and 15.4×10^{-3} for the upper and lower curves, respectively, i.e., for 410 and 290 MHz, respectively. Since the velocity of longitudinal sound propagated parallel to $[10\bar{1}0]$ is $V_{11}=6.036\times10^5$ cm/sec, these yield electron mean free paths of $l_{410}=1.4$ mm and $l_{290}=1.35$ mm; the fact that these are identical within experimental error demonstrates that the differences in the two data traces shown in Fig. 6 are consistent with our understanding of the frequency dependence of the acoustic attenuation.

To understand the physical origin of the scattering mechanisms that determine this mean free path it is important to note that the sample thickness was only 1.9 mm. Thus the value of $l\approx1.4$ mm indicates that the predominant scattering mechanism which limits the electron mean free path is scattering from the surfaces of the sample.[20] In order for the bulk electron mean free path to be unimportant it must be somewhat larger than 2 mm.

When the temperature was reduced from 4.2 to about 2.5 °K, the fractional half-width of the resonance line decreased by 4%, indicating a new mean free path for 290 MHz at 2.5 °K of 1.4 mm. If we assume that the phonon scattering has become negligible at 2.5 °K, we can deduce a mean free path for phonon scattering of $l_p=37$ mm at 4.2 °K. This mean free path is by definition the distance measured parallel to $\hat{q}$ that an electron will travel before the uncertainty in the $\hat{q}$ component of its position in real space becomes approximately $\frac{1}{2}\lambda$ as a result of scattering events. At these low temperatures practically all electron-phonon events will lead to small-angle scattering; thus at 4.2 °K the average small-angle scatter per orbit is $\pi\lambda/l_p\approx2\times10^{-3}$ rad/cycle.

The electron on its orbit actually traverses a somewhat longer path than given directly by its projection along $\hat{q}$. For the dog-bone-shaped orbit shown in Fig. 2, the total orbital path length is 2.57 times as long as the $\hat{q}$ component. Thus the actual electron-size-limited mean free path deduced from the data shown in Fig. 6 for this orbit is a bit larger than 3.6 mm. This is consistent with previous data which indicated a bulk electron mean free path at these temperatures for these samples in excess of 1 cm and in one case as large as 15 cm.

TABLE III. Experimental values of H for the resonance peaks shown in Fig. 6. H^+ and H^- refer to the upper and lower field positions of the Doppler-split pair for a single-resonance index $\bar{H}=\frac{1}{2}(H^+ + H^-)$.

n	H_n^+ (G)	H_n^- (G)	$(\bar{H})^{-1}$ ($10^{-4}\,\mathrm{G}^{-1}$)	$\lambda\bar{H}$ (G cm)
2	2426	2352	4.2	4.97
4	1216	1185	8.3	2.50
6	811	788	12.5	1.66
8	⋯	589	16.9	1.23
10	⋯	493	20.2	1.03
2	3456	3331	2.9	4.99
4	1734	1668	5.9	2.50
6	1152	1113	8.8	1.67
8	859	833	11.8	1.24
10	⋯	679	14.7	1.00
12	⋯	565	17.6	0.83

As noted earlier the second magnesium sample was strained enough to cause a detectable blur in the Laue spots of an x-ray back reflection. The electron mean free path for that sample was found to be only a little greater than 0.5 mm, a number substantially smaller than the crystal thickness of 1.8 mm. For this crystal the Doppler splitting could only be observed at the highest frequencies. Although extensive measurements were made for both crystals we will only report in the remainder of this paper data obtained with the perfect crystal.

According to Eq. (10) the extremal value of $\partial A/\partial K_H$ can be obtained from the experimental data by determining the magnetic field strength at which a Doppler-split resonance occurs together with its index n. In Table III the average position of the resonance lines in terms of H^{-1} is given together with n for the sharp Doppler-split resonances in the data shown in Fig. 6. It should be noted that the selection rules discussed in Sec. II have been invoked to determine the indexing. That is, the strong resonance at 3.4 kG in Fig. 6 has been identified as a second harmonic ($n=2$) even though no $n=1$ resonance was observed at 6.8 kG. Only even harmonics have been indexed, consistent with a twofold symmetric orbit and the appropriate restrictions for that case listed in Table I.

It is evident from the data given in Table III that the family of resonances is indeed periodic in H^{-1}; the value of the period yields a value for the extremal-area derivative of $dA/dk_1=0.80\pm0.02$ a.u. This is in excellent agreement with the value of 0.793 a.u. obtained earlier for the dog-bone orbit by band-structure calculation. The Doppler splitting of the sharp resonance at 3.4 kG shown in Fig. 6 for 410 MHz and listed in Table III is 125 ± 8 G. This would result from an effective cyclotron mass of $m^*=(0.78\pm0.05)m_0$, where m_0 is the free-electron mass; this compares very well with the theoretical prediction for this orbit described in Sec. II of $m^*=(0.78\pm0.02)m_0$. Thus there appears to be no real doubt about the certainty of the assignment of this family of resonances to the dog-bone-shaped orbit on the monster.

If we combine the experimental values for m^* and dA/dk_1 we obtain for the expectation value of the drift velocity $V_0=3.65\times10^7$ cm/sec which compares well with the value 3.73×10^7 cm/sec given in Table II. Thus all of the quantities that can be determined from a single resonance line, i.e., from its center field location and from the magnitude of the Doppler-splitting, as well as from its half-width agree *quantitatively* with the predictions of theory.

A study of an entire family of resonance lines allows further checks on the quantitative accuracy of the theory. Equation (6) predicts that the *energy* absorbed at resonance should be proportional to $\vec{V}_n\cdot\hat{q}$, where $\vec{V}_n$ is the nth Fourier coefficient of the electrons orbital velocity. Thus by comparing the amplitudes of the successive members of the family of resonances we should be able to deduce the relative values of $\vec{V}_n\cdot\hat{q}$. The y axes of the curves shown in Fig. 6 are calibrated in dB so that the amplitude attenuation coefficient can be directly determined for each harmonic. From these, by normalizing to the $n=2$ line, we obtain energy coefficients of 0, 1, 0, 0.64, 0, 0.41 for the $n=1, 2, 3, 4, 5$, and 6 lines; the corresponding ratios of the coefficients listed in Table II are 0, 1, 0, 0.645, 0, 0.344. The comparison is quite good for the odd value of n coefficients which are zero as a result of symmetry imposed restrictions. For the nonzero $n=2, 4$, and 6 coefficients, the predictions are surprisingly accurate; the quantitative agreement appears to be within experimental error. If the residual differences are significant, they probably have their origin in a $\vec{k}$ dependence of the deformation force F_0 introduced in Eq. (3), where F_0 was assumed to be independent of $\vec{k}$. For the special case under consideration here in which the acoustic wave is a pure longitudinal wave and $\vec{H}\parallel\vec{q}\parallel[10\bar{1}0]$, the magnitude of the deformation force F_0 can be expressed as a Fourier series in the cyclotron period subject to the same restrictions of twofold symmetry as V_1^n, that is, we could express $F_0(\vec{k})$ as

$$F_0(t)=\sum_{m=-\infty}^{+\infty} F_{2m}e^{i2m\omega_c t}\ . \tag{11}$$

The resonance expressed by Eq. (6) then becomes

$$\Delta E=\sum_{n=-\infty}^{+\infty}\ \sum_{n=\infty}^{+\infty}\ \frac{F_{2m}V_1^{2n}}{1/\tau+i[\omega+2(n+m)\omega_c-\vec{q}\circ\vec{V}_0]}\ , \tag{12}$$

in which the resonance denominator now depends on the index $r=2(n+m)$. This does not change the center-field location of a resonance line, its Doppler splitting, or line shape. What changes is the relative amplitude of the successive resonances. For example, the $r=2$ resonance contains the terms $n=1$, $m=0$ and $n=0$, $m=1$; thus the energy absorbed at resonance is proportional to the sum $V_1^2F_0+V_1^0F_2$ instead of just $V_1^2F_0$ as in the case of a constant deformation force. The $r=4$ resonance will contain terms involving F_0, F_2, and F_4. By carefully determining the relative amplitude attenuation coefficients for an entire family of resonances one could, in principle, determine the Fourier components of $F_0(t)$ provided one had independent values for the Fourier components of the electron velocity. We will not attempt to determine the higher Fourier coefficients of $F_0(t)$ in this paper, since the quantitative predictions of a constant deformation force are in reasonable agreement with the experimental data within our present experimental uncertainties.

In addition to the measurements made with $\vec{H}$ parallel to $\vec{q}$, measurements were also taken when $\vec{H}$ was rotated away from $\vec{q}$ in both the (0001) and $(11\bar{2}0)$ planes. The dog-bone resonance was readily followed for rotation angles ψ as large as 20° between $\vec{H}$ and $\vec{q}$. Table IV lists the values of $\partial A/\partial k_1$ determined for various values of ψ in these two planes and compares them with theoretical predictions.

When $\vec{H}$ was rotated in the (0001) plane, a symmetrically equivalent dog-bone orbit was observed for $45°\leq\psi\leq 70°$. When $\psi=60°$, $\vec{H}$ was along a symmetrically equivalent $\langle 10\bar{1}0\rangle$-type axis and relative to the $\hat{1}, \hat{2}, \hat{3}$ coordinate system defined by $\vec{H}$, the dog-bone orbit that was generated was identical to that for $\vec{H}$ parallel to $\vec{q}$ at $\psi=0°$. Thus the Fourier coefficients of the electron orbital velocity are still given by those in Table II; from the electrons reference frame the change is in the direction of $\vec{q}$ relative to the $\hat{1}, \hat{2}, \hat{3}$ coordinate system. In this particular case, $\hat{q}=\cos 60°\,\hat{1}+\sin 60°\,\hat{2}$. Thus $\vec{V}_n\circ\hat{q}$ will contain both V_1^n and V_2^n components as discussed in the Sec. II. This reduces the expected amplitude for the even harmonics by a factor of 2 but, in addition, has the more important effect of generating the odd harmonics that were missing for $\vec{H}$ parallel to $\vec{q}$.

Figure 7 shows a data trace taken with $\vec{H}$ 60° from $\vec{q}$ and with both $\vec{H}$ and $\vec{q}$ along $\langle 10\bar{1}0\rangle$-type axes. Although the data are dominated by a family of geometric resonances, the Doppler-shifted acoustic cyclotron resonances arising from the dog-bone orbit are definitely manifest. The resonances

TABLE IV. Comparison of the experimental and theoretical values of $\partial A/\partial k_1$ (in a.u.) for a series of orientations of $\vec{H}$ Relative to $\vec{q}$ in the $(11\bar{2}0)$ and (0001) planes.

ψ	$(\partial A/\partial k_1)_{\text{expt}}$	$(\partial A/\partial k_1)_{\text{theor}}$
0°	0.80	0.793
6°	0.80	0.804, ψ in $(11\bar{2}0)$ plane
11°	0.89	0.845
16°	0.94	0.915
0°	0.80	0.793
2.5°	0.80	0.796
5°	0.82	0.805, ψ in (0001) plane
7°	0.85	0.821
9°	0.85	0.843
13°	0.87	0.865

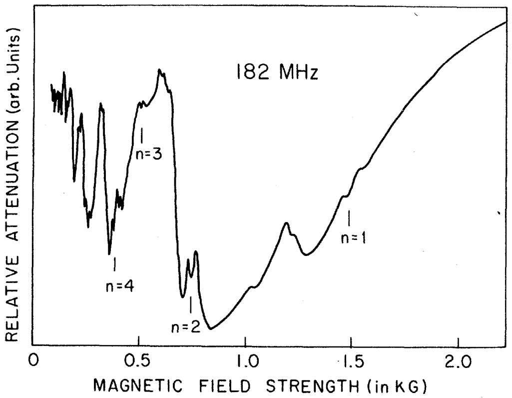

FIG. 7. Relative attenuation of 182-MHz longitudinal sound waves as a function of magnetic field strength for $\vec{q}$ along one ⟨10$\bar{1}$0⟩-type axis and $\vec{H}$ along a different ⟨10$\bar{1}$0⟩-type axis. The location of the $n = 1$, 2, 3, and 4 dog-bone resonances are indicated.

are indexed according to harmonic number; the previously missing odd harmonics are now present at their predicted value of H. All of the resonance lines occur at a lower field than they did at this frequency for $\vec{H}$ parallel to $\vec{q}$. In fact, the field value at which they occur is reduced by cos60° as predicted by Eq. (10).

It is impossible to accurately determine the relative amplitude attenuation for the resonances in Fig. 7 since they occur on a too rapidly changing background. Thus we cannot make quantitative comparisons of the amplitudes of successive resonances with theoretical predictions as we did earlier for $\vec{H}$ parallel to $\vec{q}$. We note, however, that the purely qualitative manifestation of the odd harmonics removes any residual doubt about the correctness of the harmonic indexing discussed earlier in connection with Fig. 6.

When $\vec{H}$ is rotated away from ⟨10$\bar{1}$0⟩, the twofold symmetry of the dog-bone orbit is broken and the symmetry restrictions on the V_l^n are removed. As $\vec{H}$ is rotated slowly away from $\vec{q}$ in the (0001) or (11$\bar{2}$0) plane, the amplitude of the odd harmonics will grow from zero as the orbit shape slowly deforms; also contributing to the amplitude growth of the odd harmonics is the slowly increasing projection of the V_2^n or V_3^n components in the direction of $\vec{q}$ as was demonstrated in Fig. 7. For $\psi \le 10°$ the amplitudes of the odd harmonics are small compared with the amplitudes of the even harmonics. For $\psi \ge 15°$ the even and odd harmonic amplitudes are comparable.

Figure 8 shows three data traces for $\vec{H}$ rotated away from $\vec{q}$ toward the ⟨0001⟩ crystal axis. The three data traces were taken at 4.2 °K with 410 MHz. The top trace is for $\psi = 10°$; the bottom trace is for $\psi = 20°$. The resonances have been indexed according to our previous identification. At $\psi = 10°$ there is little evidence of the odd harmonics; at $\psi = 15°$ the $n = 3$ and $n = 5$ amplitudes have become quite large while the $n = 2$ has decreased and the $n = 4$ has disappeared; at $\psi = 20°$ both the $n = 2$ and $n = 4$ resonances have virtually disappeared while the $n = 3$, $n = 5$, and $n = 7$ resonances are fairly large.

It is quite clear from the data shown in Fig. 8 that one must use extreme care in identifying and indexing members of a family of Doppler-shifted acoustic cyclotron resonances. One could very easily have concluded that the disappearance of the $n = 2$ and $n = 4$ resonance lines coincided with the disappearance of a particular family of resonances while at the same time concluding that the new $n = 3$ and $n = 5$ resonances resulted from new families of resonances with different indexing. *This is particularly probable since for most experiments the higher harmonic effects usually have successively smaller amplitudes than the lower harmonic effects. The Doppler-shifted acoustic cyclotron-resonance experiment is somewhat unusual in that the successive resonances correspond to a Fourier analysis of the periodic electron orbital velocity.*

Although the resonances arising from the dog-bone orbit tend to dominate the acoustic attenuation for fields near [10$\bar{1}$0], other weaker families of apparent resonances also are manifest in the data (see Figs. 6 and 8, for example). Note, however, that all of these other apparent resonances show up in the data as small bumps which do not exhibit Doppler splitting. The orbit-area calculations showed only one region for which $A(k_1)$ had an inflection point as a function of k_1; that region is associated with the Doppler-shifted acoustic cyclotron resonance for the dog-bone orbit discussed above. There are in addition, however, several other re-

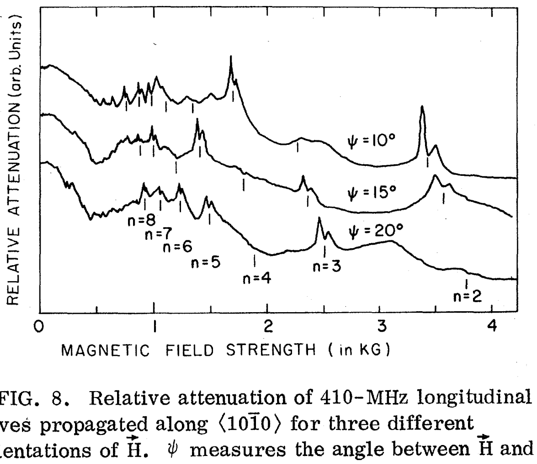

FIG. 8. Relative attenuation of 410-MHz longitudinal waves propagated along ⟨10$\bar{1}$0⟩ for three different orientations of $\vec{H}$. ψ measures the angle between $\vec{H}$ and $\vec{q}$ in the (11$\bar{2}$0) plane. The various harmonic resonances of the dog-bone orbit are indicated.

gions of the Fermi surface for which $\partial A(k_1)/\partial k_1$ varies only slowly with k_1; we have associated these regions with the families of apparent resonances that remain in the data. We have tentatively identified some of these families with orbits on the monster, clam, and butterflies.[8] Of these, one family in particular arises from regions of the Fermi surface having an average value of $\partial A/\partial k$ somewhat larger than all the others. When H is along $[10\bar{1}0]$ these orbits occur on the monster in the range $0.51 \leq k_1 \leq 0.54$ a.u. $A(k_1)$ in this region is shown in Fig. 3; its slope varies by about 10% around an average value of $\partial A/\partial k = 0.60$ a.u. over the range of k_1 listed above. The particular orbits that are involved are the continuation of the two halves of the dog-bone orbit after it has been cut in two by the saddle point at $k_1 = 0.470$ a.u. One of the two orbits of this type would have twofold symmetry if $\vec{H}$ were placed along one of the $\langle 11\bar{2}0\rangle$-type axes 30° on either side of $\vec{q}$; the other would have twofold symmetry when $\vec{H}$ was placed along the other $\langle 11\bar{2}0\rangle$-type axis. Theory predicts that the average value of $\partial A/\partial k_1$ for this orbit increases as the angle increases between $\vec{H}$ and the appropriate $\langle 11\bar{2}0\rangle$-type axis. Thus when $\vec{H}$ is near $[10\bar{1}0]$ the data consist of two different families of apparent resonances; when $\vec{H}$ is exactly parallel to $[10\bar{1}0]$ the apparent resonances are degenerate; the degeneracy is removed as $\vec{H}$ is rotated from $[10\bar{1}0]$ toward one of the $\langle 11\bar{2}0\rangle$ axes.

The data showing the $n = 1$ attenuation peak of these two families are presented in Fig. 9 for a series of orientations in the (0001) plane of $\vec{H}$ relative to $\langle 10\bar{1}0\rangle$. The degeneracy at $\psi = 0°$ and its splitting for $\psi \neq 0°$ is apparent.

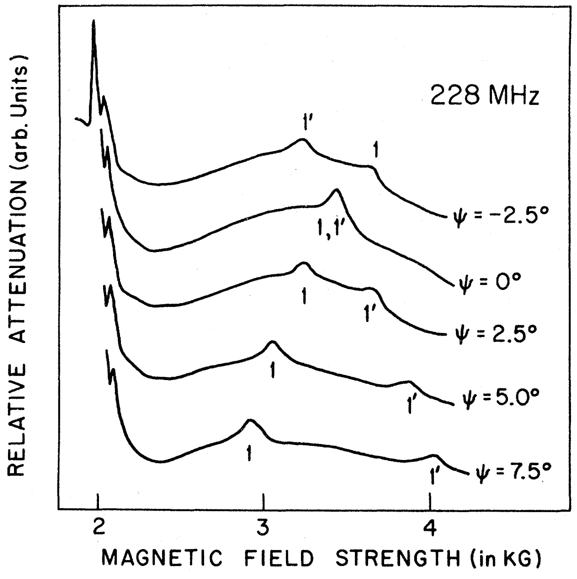

FIG. 9. $n = 1$ resonances of two families of "apparent" resonances for 410-MHz longitudinal waves. The $n = 2$ dog-bone resonance is also shown. Note that the apparent resonances do not exhibit Doppler splitting and that they are degenerate at $\psi = 0°$.

The location of the peak at $\psi = 0°$ in Fig. 9 corresponds to a value of $\partial A/\partial k_1$ of about 0.7 a.u. The data, however, cut off rather sharply with increasing H; this cutoff likely corresponds to the orbits located in the plane containing the saddle point at $k_1 = 0.545$ a.u., where the area calculations are least accurate. At this point our area calculations yield a value of $\partial A/\partial k_1 = 0.67$ a.u. which is in reasonable agreement with the experimental number. Note the complete lack of any Doppler splitting in the resonance line. This clearly results from the fact that $A(k_1)$ for the orbits contributing this apparent resonance does not actually have an inflection point. If the electron mean free path had been larger, i.e., if we had used thicker crystals, the amplitude of these resonances would decrease relative to the resonances for the dog-bone orbit.

V. CONCLUSIONS

The results of our study of the Doppler-shifted acoustic cyclotron resonance for longitudinal sound waves propagated along the $\langle 10\bar{1}0\rangle$ axis of magnesium are in excellent quantitative agreement with the predictions of theory. Our previous knowledge of the energy band structure for the electron quasiparticle enabled us to make quantitative predictions about the location of resonance lines, the Doppler splitting of the resonance lines, and the relative amplitudes of successive resonances in a family of resonances.

It is apparent that a more careful study of these relative amplitudes would yield information about the variation of the deformation potential around the Fermi surface. It is also apparent that a careful study of the temperature dependence of the linewidth for the dog-bone resonances will yield valuable information about the average interaction of the electrons with thermally excited phonons. This new information could then be used to test our understanding of the detailed interactions of electrons and phonons; this is particularly true for magnesium where at present we have detailed knowledge of both the electron and phonon dispersion curves.

We should also emphasize that the data for the Doppler-shifted acoustic cyclotron resonance in magnesium would not have been amenable to interpretation without first having a detailed quantitative understanding of the Fermi surface of magnesium. This prior understanding prevented us from making many not so obvious errors in interpreting our data as well as providing us with a considerable amount of insight into the results of our experiment.

[†] Work supported by AFOSR Grant No. 68-1479 to John Carroll University, Cleveland, Ohio, and Army Research Office (Durham) Grant No. DA-ARO-D-31-124-G926-Res to the University of Chicago, Chicago, Ill.

[1] H. E. Bömmel, Phys. Rev. 96, 220 (1954).

[2] L. Mackinnon, Phys. Rev. 98, 1181 (1955).

[3] H. E. Bömmel, Phys. Rev. 100, 758 (1955).

[4] A. B. Pippard, Phil. Mag. 46, 1104 (1955).

[5] T. Kjeldaas, Phys. Rev. 113, 1473 (1959).

[6] M. H. Cohen, M. J. Cohen, and W. A. Harrison, Phys. Rev. 117, 937 (1960).

[7] A. B. Pippard, Proc. Roy. Soc. (London) A257, 165 (1960).

[8] J. B. Ketterson and R. W. Stark, Phys. Rev. 156, 748 (1967).

[9] R. W. Stark, Phys. Rev. 162, 589 (1967).

[10] B. K. Jones, Phil. Mag. 9, 217 (1964).

[11] B. I. Miller, Phys. Rev. 151, 519 (1966).

[12] J. A. Munarin, Phys. Rev. 172, 737 (1968).

[13] G. I. Kotkin, Zh. Eksperim. i Teor. Fiz. 41, 281 (1961)[Soviet Phys. JETP 14, 210 (1962)].

[14] J. C. Kimball, R. W. Stark, and F. M. Mueller, Phys. Rev. 162, 600 (1967).

[15] P. Roach and R. W. Stark (unpublished).

[16] For an excellent general discussion of the physical concepts of interacting conduction electrons and sound waves in the presence of an applied magnetic field the interested reader is referred to Ref. 7. The discussion given in this paper follows from that work as well as from Ref. 10.

[17] W. A. Harrison, Phys. Rev. 118, 1190 (1960).

[18] For a block diagram of the essential apparatus see R. V. Kollarits, J. Trivisonno, and R. W. Stark, Phys. Rev. B 2, 1508 (1970).

[19] J. Davenport, J. Hunter, and R. Leskovec, Rev. Sci. Instrum. 41, 1426 (1970).

[20] Figure 7 of Ref. 18 shows that the electron mean free path determined for this same crystal at 4.2 °K from open-orbit resonance studies is also 1.4 mm. This same figure shows that at 1.2 °K the electron mean free path is 1.8 mm which is essentially the crystal length.

PHYSICAL REVIEW B VOLUME 3, NUMBER 8 15 APRIL 1971

Lattice Conductivity, Lorenz Numbers, and Nernst-Ettingshausen Effect in Tungsten at Liquid-Helium Temperatures*

Jerome R. Long
*Department of Physics, Virginia Polytechnic Institute and State University,
Blacksburg, Virginia* 24061

(Received 26 August 1970)

A further analysis of previously published measurements of the dc electrical and thermal transport coefficients of a tungsten crystal is presented. The coefficients were measured as functions of a strong magnetic field at several temperatures in the range of liquid He^4. Problems in separating the lattice thermal conductivity from the electronic thermal conductivity by a simultaneous study of the magnetoresistivities are discussed. The limiting conductivity obtained from such a study of the tungsten data is found to be in reasonable agreement with calculations based on the assumption of strongly coupled phonons scattered by nearly free electrons. From the same data, the Lorenz number is deduced as a function of temperature and found to be in excellent agreement with an electron-electron scattering formula given by Ziman. The transverse (Hall and Righi-Leduc) conductivities are used to deduce a transverse Lorenz number which displays an unexpected temperature dependence that is not explained. An apparent phonon drag effect, very similar to that found by Long *et al.* in the transverse (Nernst-Ettingshausen) thermoelectric coefficient of antimony, is found in the tungsten data for the same coefficient, and is quantitatively explained by a simple model. An electronic specific-heat coefficient is also deduced from the Nernst-Ettingshausen data, and is found to have a value intermediate to the results of augmented-plane-wave (APW) and relativistic augmented-plane-wave (RAPW) Fermi surface calculations.

I. INTRODUCTION

A recent paper[1] presented the results of an experimental determination of six dc electrical and thermal transport coefficients in a tungsten crystal at liquid-helium temperatures in a strong magnetic field. In that paper, the behavior of each kinetic coefficient was discussed independently of the other kinetic coefficients. In this paper, relationships between several of the coefficients are examined. It is only by studying these relationships that the data take on very much relevance. In Secs. II and III, the simultaneous behavior of the electrical and thermal magnetoconductivity tensors is studied, the object in Sec. II being to obtain the lattice conductivity, and in Sec. III, the Lorenz numbers of the lon-

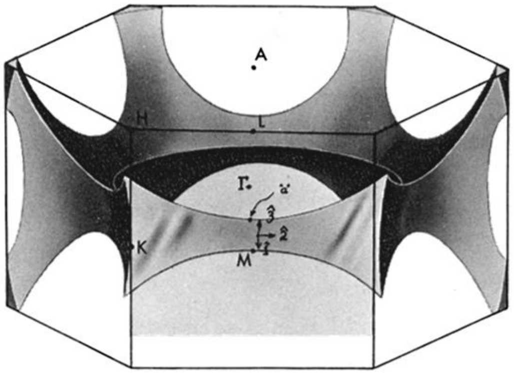

FIG. 2. Portion of the second-band hole surface, the monster, showing the location of a typical dog-bone-type orbit. The $\hat{1}$, $\hat{2}$, $\hat{3}$ coordinate system is defined in the text.